Electrical resistivity and thermal conductivity of liquid Fe alloys at high *P* and *T*, and heat flux in Earth's core

Nico de Koker[1], Gerd Steinle-Neumann, and Vojtěch Vlček

Bayerisches Geoinstitut, Universität Bayreuth, D-95440 Bayreuth, Germany

Earth's magnetic field is sustained by magnetohydrodynamic convection within the metallic liquid core. In a thermally advecting core, the fraction of heat available to drive the geodynamo is reduced by heat conducted along the core geotherm, which depends sensitively on the thermal conductivity of liquid iron and its alloys with candidate light elements. The thermal conductivity for Earth's core is very poorly constrained, with current estimates based on a set of scaling relations that were not previously tested at high pressures. We perform first-principles electronic structure computations to determine the thermal conductivity and electrical resistivity for Fe, Fe–Si, and Fe–O liquid alloys. Computed resistivity agrees very well with existing shock compression measurements and shows strong dependence on light element concentration and type. Thermal conductivity at pressure and temperature conditions characteristic of Earth's core is higher than previous extrapolations. Conductive heat flux near the core–mantle boundary is comparable to estimates of the total heat flux from the core but decreases with depth, so that thermally driven flow would be constrained to greater depths in the absence of an inner core.

electronic transport | Kubo–Greenwood | planetary magnetism

The generation of the Earth's magnetic field is directly coupled to the thermal evolution of the liquid outer core, the cooling of which is modulated by heat flux from the core into the base of the mantle (1–6). In a simple thermally driven core, as, for example, in the absense of a crystallizing inner core and associated latent heat release and chemical buoyancy, heat transported by conduction is not available to drive the geodynamo. Knowledge of its relative contribution to thermal transport in the core is therefore critical to understanding the long term stability of Earth's magnetic field, which has been present as far back as 3.45 billion years ago (7), when the core was likely too hot for a solid inner core to crystallize (1, 4).

Existing estimates of thermal conductivity (k_{el}) and electrical resistivity (ρ_{el}) of Earth's outer core are based on extrapolations (8, 9) of resistivity measurements in shock-compressed Fe and Fe–Si alloys (10–12) to core temperatures and pressures. These extrapolations assume the direct proportionality of electrical resistivity to temperature, its invariability along and across the Fe liquidus, and adherence to the Wiedemann–Franz law, which relates electrical resisitivity and thermal conductivity for metals through the Lorenz number (13) $\lambda_0 = k_{el}\rho_{el}/T = 2.44 \times 10^{-8} \text{ W}\Omega/\text{K}^2$. No data are available for Fe alloys of the other candidate light elements that have been proposed to account for the seismically observed density deficit of Earth's core relative to pure Fe (14). Previous high-pressure studies of the electronic transport properties of Fe at high pressure (15–18) were limited to low temperatures. Clearly, there is a need for direct determination of electrical resistivity and thermal conductivity of ferro-metallic liquids at pressures and temperatures characteristic of Earth's outer core.

We compute k_{el} and ρ_{el} for Fe, Fe$_7$Si, Fe$_3$Si, Fe$_7$O, and Fe$_3$O liquid alloys (6.7, 14.3 wt% Si; 3.9, 8.7 wt% O) from first princi-

ples, using density functional theory and the Mermin functional to determine finite temperature equilibrium charge density and electronic structure (19–21). First-principles molecular dynamics (FPMD) simulations are performed in the canonical ensemble for temperatures of 2,000–8,000 K and volumes corresponding to pressures of 0–360 GPa. Electronic transport properties are subsequently computed for a series of uncorrelated snapshots from the FPMD simulations using the Kubo–Greenwood equation (22, 23) (see *Methods*), which expresses the electronic Onsager coefficients L_{ij} directly in terms of the expectation values of the electronic velocity operator (24).

Computed resistivities for pure Fe liquid (Fig. 1) closely agree with the shock compression measurements of Keeler (10) and the lowest pressure point of Bi et al. (11), at pressures where Hugoniot temperatures (25) are comparable to those in our simulations. Similarly, values for Fe$_3$Si liquid are in agreement with the shock measurements of Matassov (12) for the same composition. Lower pressure shock compression measurements are at progressively lower temperatures; the 18 GPa measument of Keeler (10) is at 320 K, and agrees well with room temperature static measurements in hcp Fe (17, 18), adding confidence to the shock compression resistivity data, and our results. In light of the large scatter in the Bi et al. (11) dataset, and the serious disagreement between the data of Bi et al. (11) and Keeler (10) above 120 GPa, we feel that comparison of our results with the measurements of Keeler (10) is more appropriate. Computed low pressure resistivity for pure Fe liquid is somewhat smaller than experimental values (26, 27), yet computed ambient pressure thermal conductivity does agree closely with experimental estimates for liquid Fe at temperatures above melting (1,810 K) (28).

In drawing comparisons to the shock compression resistivity measurements, we assume that the resistivity of liquid and solid metal phases are similar, which is known to be the case for Fe at low pressure (26, 27). In our comparison of thermal conductivities, we further assume the electronic contribution to heat transport to be much larger than that due to transport by phonons alone. In Fe liquid at ambient pressure, the latter is estimated to be about 3 W/m K (8), much smaller than the experimental total conductivity of 40.3 W/m K (28).

In contrast with previous assumptions for Earth's core (8, 9), we find that the validity of the Wiedemann–Franz relation depends strongly on temperature and composition. At core temperatures, computed Lorenz numbers for Fe and Fe–Si liquids are in the range of 2.2–2.4 $\times 10^{-8}$ WΩ/K^2; alloying of liquid Fe with O results in a notable decrease in λ, with values as low as 1.8 $\times 10^{-8}$ WΩ/K^2 for Fe$_3$O liquid at high pressure and temperture. This deviation from the Wiedemann–Franz relation sug-
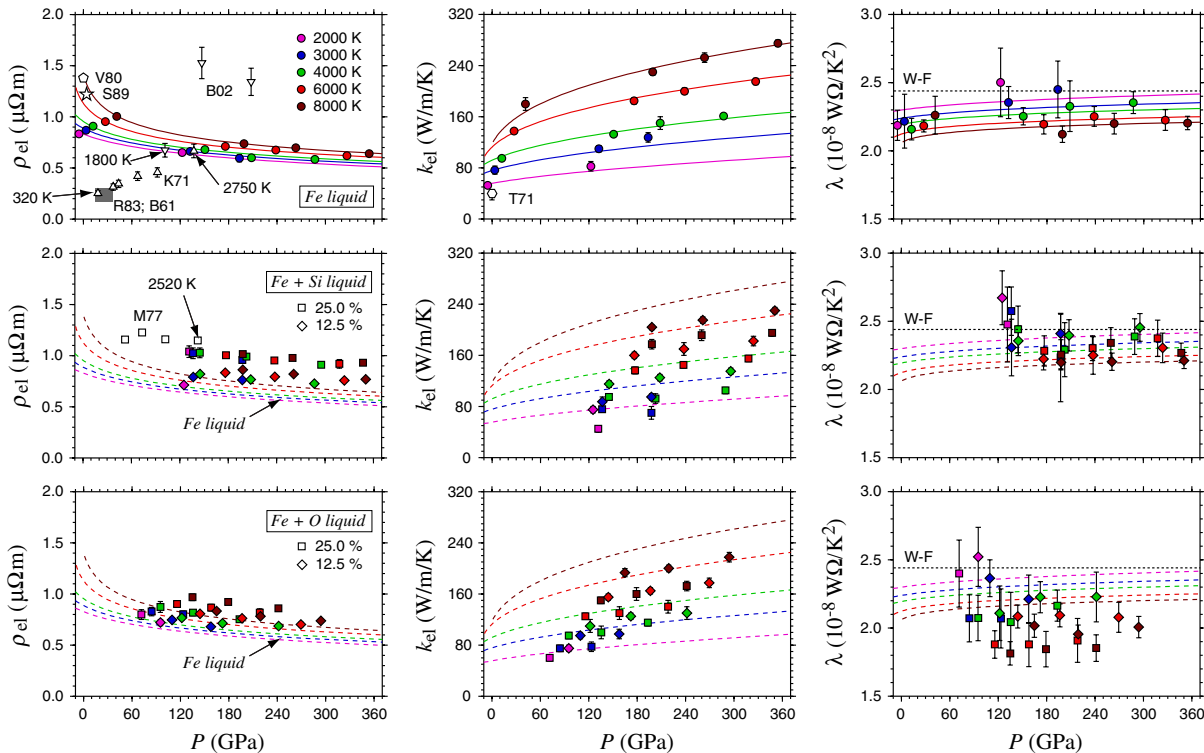
Fig. 1. Computed electrical resistivity (ρ_{el}), thermal conductivity (k_{el}), and corresponding Lorenz numbers (λ). Solid lines (top row) and dashed lines (middle and bottom rows) show the Bloch–Grüneisen models of Fe liquid; the horizontal dotted line indicates the value of the Lorenz number expected via the Wiedemann–Franz relation (W-F). Hugoniot temperatures (25) for selected shock compression datapoints [K71 (10), M77 (12), B02 (11)] are shown to guide comparisons. Other experimental data (see text): R83 (17), B61 (18), T71 (28), S89 (27), V80 (26).

gests that electron scattering in Fe–O liquid alloys is strongly anelastic, resulting in a breakdown of the simple relaxation time picture of electronic migration.

We find electrical resistivity to vary linearly with temperature, consistent with the prediction of the Bloch–Grüneisen equation for systems where electrons are primarily scattered by phonons. However, ρ_{el} is not directly proportional to T (Fig. 2), as is assumed in the oft-used extrapolations of experimental measurements to core conditions (8, 9). Augmenting the Bloch–Grüneisen formalism (29), we construct model descriptions for k_{el} and ρ_{el} as a function of volume and temperature for the different
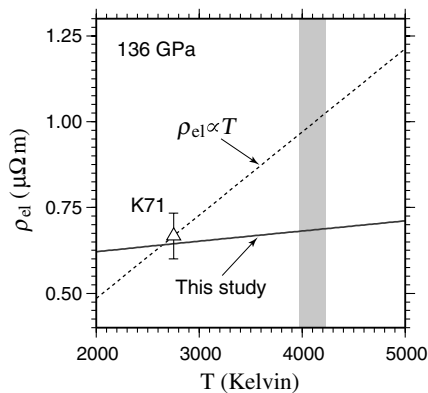

Fig. 2. Temperature dependence of electrical resistivity for pure Fe liquid at 136 GPa, determined using the model in Table 1 (solid red line), agrees very well with the resistivity measurement of Keeler (10) at the same pressure. Stacey and Anderson (8) used $\rho_{el} \propto T$ (dashed line) in their extrapolation of this measurement to temperatures of the core near the core–mantle boundary. The shaded region indicates the T range near the core–mantle boundary from the range of candidate adiabats used (see text).

liquid phases considered (Table 1; see *Methods*). Combining these models with a pressure–volume–temperature equation of state for conductive liquids (30), we derive ρ_{el} and k_{el} values along a set of candidate adiabatic thermal profiles for Earth's core, derived from the range of Fe-melting temperatures (25, 31, 32).

Our k_{el} values for the outer core are notably higher than previous extrapolations [Fig. 3; 30–60 W/m K (8, 9)], reflecting the incorrect temperature dependence of resistivity assumed in earlier studies (Fig. 2). As a consequence, our predicted conductive heat flux at the top of the core is 14–20 TW, larger than the 5–15 TW of total heat flux across the core–mantle boundary inferred from intraplate volcanism (5). A lower heat flux at the top of the core would require a smaller k_{el}, which can be obtained through a larger concentration of light elements in this region. Indeed, an anomalous light element fraction at the top of the core has been proposed on dynamical grounds (33) and is supported by seismic observations (34). However, because this concentration of light elements likely results from inner core crystallization and the associated chemical buoyancy, the difficulty posed by a large conductive heat flux remains, especially in the absence of a crystallizing inner core.

Table 1. k_{el} and ρ_{el} model parameters for Eq. 5

	Fe	Fe$_7$Si	Fe$_3$Si	Fe$_7$O	Fe$_3$O
ρ_{0R}, $\mu\Omega$m	0.77	0.84	1.26	0.85	1.00
ρ_{1R}, $\mu\Omega$m	0.084	0.13	0.0015	0.090	0.12
λ_R, WΩ/K^2	2.25	2.34	2.40	2.24	2.11
a	0.77	0.41	0.69	0.59	0.83
b	1.29	2.92	4.10	2.02	0.99
c	−0.078	−0.13	−0.016	−0.053	−0.069
d	−0.057	−0.12	−0.057	−0.096	−0.17

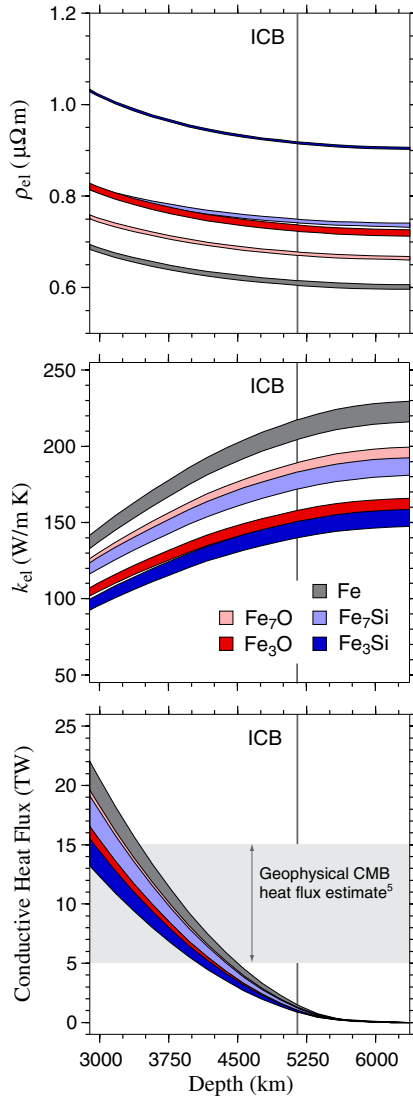In all cases, $T_R = 3{,}000$ K and $V_R = 7.0$ cm^3/atom.

Fig. 3. (*Top*) Electrical resistivity and (*Middle*) electronic thermal conductivity for the various compositions considered in this study, evaluated using the models in Table 1 along a range of candidate core adiabats (see text). (*Bottom*) Corresponding heat flux values computed as $4\pi r^2 k_{\text{el}} \nabla T$, where r is the radius, compared to geophysical estimates of core–mantle boundary (CMB) heatflux (5).

Model conductive heat flux decreases rapidly with depth in the core, primarily due to the spherical geometry. Excluding the possible effects of radiogenic heating and latent heat released through inner core crystallization, conservation of energy requires total heat flux to remain constant throughout the core. The fraction of the total heat flux transported via convection would therefore increase with depth, suggesting that thermally driven flow would occur mainly within the deeper portion of the liquid core.

Methods

First-Principles Simulations. The method used to compute electronic transport properties is similar to that of refs. 22 and 23. Born–Oppenheimer molecular dynamics (FPMD) is performed using the VASP code (35). To test for finite size effects, we consider system sizes of 64, 128, 144, and 192 atoms (see below). The exchange-correlation potential is represented in the generalized gradient approximation (GGA-PBE) (36), with valence electrons represented as planewaves with a cutoff of 300 eV in the projector augmented wave (PAW) formalism (37, 38). The Brillouin zone is sampled at the Γ point only. Simulations are performed in the *NVT* ensemble for volumes V/V_X = 1.0, 0.7, 0.65, and 0.6, where V_X = 7.121 cm³/mol atom, and temperatures of 2,000, 3,000, 4,000, 6,000 and 8,000 K, and cover

at least 20 ps of simulation time. The time dependent mean square displacement is used to check that systems are indeed in the liquid state.

From each FPMD-generated phase trajectory, we extract atomic configuration snapshots every 1,000 fs (i.e., 20 per *P–T* point) for which we compute the electrical resistivity (ρ_{el}) and thermal conductivity (k_{el}). Velocity autocorrelation functions (39) for our simulations all decay within 250 fs, indicating that a 1,000-fs time separation is sufficient for individual snapshots to be uncorrelated. In this way a representative sampling of the liquid structure at each *P–T* point is obtained.

Electronic transport properties ρ_{el} and k_{el} are computed using the Kubo–Greenwood equation, as implemented in the Abinit code (22, 40). The equation, which follows from the electronic current autocorrelation function via Kubo's linear response formalism, is

$$L_{ij} = (-1)^{(i+j)} \frac{he^2}{V_{\text{cell}}} \sum_{k',k} \lim_{\epsilon \to 0} \frac{f(\epsilon_{k'}) - f(\epsilon_k)}{\epsilon} \delta(\epsilon_{k'} - \epsilon_k - \epsilon)$$

$$\times \langle \psi_k | \hat{\mathbf{v}} | \psi_{k'} \rangle \langle \psi_{k'} | \hat{\mathbf{v}} | \psi_k \rangle (\epsilon_{k'} - \epsilon_F)^{i-1} (\epsilon_k - \epsilon_F)^{j-1}, \quad \textbf{[1]}$$

$$\rho_{\text{el}} = 1/L_{11}, \quad \textbf{[2]}$$

$$k_{\text{el}} = \frac{1}{e^2 T} \left(L_{22} - \frac{L_{12}^2}{L_{11}} \right). \quad \textbf{[3]}$$

In Eqs. **1–3** ϵ_F is the Fermi energy; ψ_k, ϵ_k, and $f(\epsilon_k)$ are the wave function, eigenvalue, and Fermi–Dirac occupation of eigenstate k, respectively; $\hat{\mathbf{v}}$ is the velocity operator; and V_{cell} is the simulation cell volume. For a given snapshot, the self-consistent electronic relaxation is performed for electronic temperature equal to the ionic temperature via the Mermin functional (21). ψ_k and ϵ_k are represented by the Kohn–Sham eigenfunctions and eigenvalues for each given snapshot, while $\hat{\mathbf{v}}$ is computed from the Hamiltonian gradient, $h\hat{\mathbf{v}} = 2\pi \partial \hat{H}/\partial \mathbf{k}$.

Cells of 144 atoms for Fe and 128 atoms for Fe–Si and Fe–O alloys are used in production runs; test simulations with 192 atoms at V/V_X = 0.6 and 1.0 for T = 8,000 K yielded transport coefficients within 1% of the values determined with the smaller systems. To avoid core charge overlap in the linear response calculations at high degrees of compression, we constructed GGA-PAW atomic potentials with small cutoff radii (0.9 Å for Fe and Si, 0.53 Å for O) (36, 41). A planewave basis set cutoff of 400 eV is found to yield converged electronic transport coefficients. Production runs sample the Brillouin zone only at the Γ-point. This choice is appropriate in large simulation cells, where the Brillouin zone edge is effectively folded into its center. Test values computed using a $2 \times 2 \times 2$ Monkhorst–Pack **k**-point grid (42) at V/V_X = 0.6 and 1.0 for T = 8,000 K vary by no more than 5% from the single **k**-point results.

It should be noted that the Kubo–Greenwood equation determines the electronic transport properties directly from the self-consistent electronic structure within the Born–Oppenheimer approximation. Ionic and electronic scattering are implicitly included in the computation, but electron–phonon coupling is not described. The approach is therefore well suited to characterizing high temperature electronic transport coefficients, especially in liquid metals.

***P-T* Model for ρ_{el} and k_{el}.** We represent the temperature and volume dependence of electrical resistivity via the Bloch–Grüneisen equation, with volume dependence included through a power law dependence of the prefactor (29)

$$\rho_{\text{el}}(V,T) = \rho_{0R} \left[\frac{V}{V_R} \right]^a + \rho_{1R} \left[\frac{V}{V_R} \right]^b \frac{T}{T_R}, \quad \textbf{[4]}$$

where a and b are constants that include volume dependence of the vibrational frequencies. The electronic thermal conductivity is represented self-consistently through the Lorenz number using

$$k_{\text{el}}(V,T) = \frac{\lambda(V,T)T}{\rho_{\text{el}}(V,T)}, \quad \textbf{[5]}$$

by fitting the computed Lorenz numbers to

$$\lambda(V,T) = \lambda_R \left[\frac{V}{V_R} \right]^c \left[\frac{T}{T_R} \right]^d. \quad \textbf{[6]}$$

For the Fe liquid alloys we consider, reference volume and temperature are chosen as T_R = 3,000 K and V_R = 7.0 cm³/mol atom. Values for ρ_{0R}, ρ_{1R}, λ_R, a, b, c, and d for each of the simulated systems is given in Table 1.

1. Buffett BA, Huppert H, Lister JR, Woods AW (1992) Analytical model for the solidification of the Earth's core. *Nature* 356:329–331.
2. Glatzmaier GA, Coe RS, Hongre L, Roberts PH (1999) The role of the Earth's mantle in controlling the frequency of geomagnetic reversals. *Nature* 401:995–890.
3. Gubbins D, Alfé D, Masters G, Price GD, Gillan MJ (2003) Can the Earth's dynamo run on heat alone? *Geophys J Int* 155:609–622.
4. Nimmo F (2007) Thermal and compositional evolution of the core. *Treatise of Geophysics*, ed DJ Stevenson (Elsevier, Amsterdam), Vol 9: Evolution of the Earth, pp 217–241.
5. Lay T, Hernlund J, Buffett BA (2008) Core-mantle boundary heat flow. *Nat Geosci* 1:25–32.
6. Sakuraba A, Roberts PH (2009) Generation of a strong magnetic field using uniform heat flux at the surface of the core. *Nat Geosci* 2:802–805.
7. Tarduno JA, et al. (2010) Geodynamo, solar wind, and magnetopause 3.4 to 3.45 billion years ago. *Science* 327:1238–1240.
8. Stacey FD, Anderson OL (2001) Electrical and thermal conductivities of Fe-Ni-Si alloy under core conditions. *Phys Earth Planet Interiors* 124:153–162.
9. Stacey FD, Loper DE (2007) A revised estimate of the conductivity of iron alloy at high pressure and implications for the core energy balance. *Phys Earth Planet Interiors* 161:13–18.
10. Keeler RN (1971) Electrical conductivity of condensed media at high pressures. *Physics of High Energy Density*, eds P Caldirola and H Knoepel (Academic, New York), Vol 48, pp 106–125.
11. Bi Y, Tan H, Jing F (2002) Electrical conductivity of iron under shock compression up to 200 GPa. *J Phys Condens Matter* 14:10849–10854.
12. Matassov G (1977) The electrical conductivity of iron-silicon alloys at high pressure and the earth's core. PhD thesis (University of California).
13. Ashcroft NW, Mermin ND (1976) *Solid State Physics* (Saunders College, Philadelphia), 1st Ed.
14. Birch F (1952) Elasticity and constitution of the Earth's interior. *J Geophys Res* 57:227–286.
15. Konôpková Z, Lazor P, Goncharov AF, Struzhkin VV (2011) Thermal conductivity of hcp iron at high pressure and temperature. *High Press Res* 31:228–236.
16. Sha X, Cohen RE (2010) First-principles studies of electrical resistivity of iron under pressure. *J Phys Condens Matter* 23, 10.1088/0953-8984/23/7/075401.
17. Reichlin R (1983) Measuring the electrical resistance of metals to 40 GPa in the diamond-anvil cell. *Rev Sci Instrum* 54:1674–1677.
18. Balchan A, Drickamer H (1983) High pressure electrical resistance cell, and calibration points above 100 kilobars. *Rev Sci Instrum* 32:308–313.
19. Hohenberg P, Kohn W (1964) Inhomogeneous electron gas. *Phys Rev* 136:864–871.
20. Kohn W, Sham LJ (1965) Self-consistent equations including exchange and correlation effects. *Phys Rev* 140:1133–1138.
21. Mermin ND (1965) Thermal properties of inhomogeneous electron gas. *Phys Rev* 137:1441–1443.
22. Recoules V, Crocombette J.-P (2005) Ab initio determination of electrical and thermal conductivity of liquid aluminum. *Phys Rev B* 72, 10.1103/PhysRevB.72.104202.
23. Holst B, French M, Redmer R (2011) Electronic transport coefficients from ab initio simulations and application to dense liquid hydrogen. *Phys Rev B* 83, 10.1103/PhysRevB.83.235120.
24. Ziman JM (1960) *Electrons and Phonons* (Oxford Univ Press, Oxford).
25. Brown JM, McQueen RG (1986) Phase transitions, Grüneisen parameter, and elasticity for shocked iron between 77 GPa and 400 GPa. *J Geophys Res* 91:7485–7494.
26. Zytveld JBV (1980) Electrical resistivities of liquid transition metals. *J Phys Colloques* 41:503–506.
27. Secco RA, Schloessin HH (1989) The electrical resistivity of solid and liquid Fe at pressures up to 7 GPa. *J Geophys Res* 94:5887–5894.
28. Touloukian YS, Powell RW, Ho CY, Klemens PG (1971) *Thermophysical Properties of Matter. Volume 1. Thermal Conductivity—Metal Elements and Alloys* (IFI/Plenum, New York).
29. Dugdale JS, Gugan D (1962) The effect of pressure on the electrical resistance of lithium, sodium and potassium at low temperatures. *Proc R Soc Lond A* 270:186–211.
30. de Koker N, Stixrude L (2009) Self-consistent thermodynamic description of silicate liquids, with application to shock melting of MgO periclase and MgSiO$_3$ perovskite. *Geophys J Int* 178:162–179.
31. Ma YZ, et al. (2004) In situ X-ray diffraction studies of iron to Earth-core conditions. *Phys Earth Planet Interiors* 143-144:455–467.
32. Alfè D (2009) Temperature of the inner-core boundary of the Earth: Melting of iron at high pressure from first-principles coexistence simulations. *Phys Rev B* 79 060101(R).
33. Buffett BA, Garnero EJ, Jeanloz R (2000) Sediments at the top of Earth's core. *Science* 290:1338–1342.
34. Helffrich G, Kaneshima S (2010) Outer-core compositional stratification from observed core wave speed profiles. *Nature* 468:807–810.
35. Kresse G, Furthmüller J (1996) Efficiency of ab-initio total energy calculations for metals and semiconductors using a plane-wave basis set. *Comput Mater Sci* 6:15–50.
36. Perdew JP, Burke K, Ernzerhof M (1996) Generalized gradient approximation made simple. *Phys Rev Lett* 77:3865–3868.
37. Blöchl PE (1994) Projector augmented-wave method. *Phys RevB* 50:17953–17979.
38. Kresse G, Joubert D (1999) From ultrasoft pseudopotentials to the projector augmented-wave method. *Phys Rev B* 59:1758–1775.
39. Allen MP, Tildesley DJ (1987) *Computer Simulation of Liquids* (Oxford Univ Press, Oxford), 1st Ed.
40. Gonze X, et al. (2005) A brief introduction to the ABINIT software package. *Zeitschrift für Kristallographie* 220:558–562.
41. Holzwarth N, Tackett A, Matthew G (2001) A projector augmented wave (PAW) code for electronic structure calculations, Part I: Atompaw for generating atom-centered function. *Comput Phys Commun* 135:329–347.
42. Monkhorst HJ, Pack JD (1976) Special points for Brillouin-zone integrations. *Phys Rev B* 13:5188–5192.

EARTH, ATMOSPHERIC, AND PLANETARY SCIENCES